Title

Inhibition of acetyl-CoA carboxylase suppresses fatty acid synthesis and tumor growth of non-small-cell lung cancer in preclinical models

Journal

Nature Medicine, 22(10)

ISSN

1078-8956

Authors

Svensson, Robert U
Parker, Seth J
Eichner, Lillian J
et al.

Publication Date

2016-10-01

DOI

10.1038/nm.4181

Peer reviewed

HHS Public Access

Author manuscript

Nat Med. Author manuscript; available in PMC 2017 March 19.

Published in final edited form as:

Nat Med. 2016 October ; 22(10): 1108–1119. doi:10.1038/nm.4181.

Inhibition of acetyl-CoA carboxylase suppresses fatty acid synthesis and tumor growth of non-small cell lung cancer in preclinical models

Robert U. Svensson[1], **Seth J. Parker**[2,$], **Lillian J. Eichner**[1,$], **Matthew J. Kolar**[3], **Martina Wallace**[2], **Sonja N. Brun**[1], **Portia S. Lombardo**[1], **Jeanine L. Van Nostrand**[1], **Amanda Hutchins**[1], **Lilliana Vera**[1], **Laurie Gerken**[1], **Jeremy Greenwood**[4], **Sathesh Bhat**[4], **Geraldine Harriman**[5], **William F. Westlin**[5], **H. James Harwood Jr.**[5], **Alan Saghatelian**[3], **Rosana Kapeller**[5,*], **Christian M. Metallo**[2,6], and **Reuben J. Shaw**[1,*]

[1]Department of Molecular and Cell Biology, The Salk Institute for Biological Studies, San Diego, La Jolla, CA, USA

[2]Department of Bioengineering, University of California San Diego, La Jolla, CA, USA

[3]Clayton Foundation Laboratories of Peptide Biology, The Salk Institute for Biological Studies, San Diego, La Jolla, CA, USA

[4]Schrödinger, New York, NY, USA

[5]Nimbus Therapeutics, Cambridge, MA, USA

[6]Moores Cancer Center, University of California San Diego, La Jolla, CA, USA

Abstract

Continuous *de novo* fatty acid synthesis is a common feature of cancer required to meet the biosynthetic demands of a growing tumor. This process is controlled by the rate-limiting enzyme acetyl-CoA carboxylase (ACC), an attractive but traditionally intractable drug target. Here, we provide genetic and pharmacological evidence that in preclinical models ACC is required to maintain *de novo* fatty acid synthesis needed for growth and viability of non-small cell lung cancer (NSCLC). We describe the ability of ND-646—an allosteric inhibitor of the ACC enzymes ACC1 and ACC2 that prevents ACC subunit dimerization—to suppress fatty acid synthesis *in vitro* and *in vivo*. Chronic ND-646 treatment of xenograft and genetically engineered mouse models of

*To whom correspondence should be addressed: shaw@salk.edu, rosana.kapeller@nimbustx.com.
$these authors contributed equally to this work

AUTHOR CONTRIBUTIONS

R.U.S and R.J.S designed the experiments and wrote the manuscript with input from all authors. R.U.S. performed all experiments except as noted. P.S.L and J.L.V.N assisted with CRISPR/Cas9 studies in Fig.1. S.J.P and C.M.M performed the FASyn analysis in Fig. 1 and Fig. 3 and with help from M.W analyzed FASyn in tumors prepared by R.U.S in Fig. 5. M.J.K. and A.S performed the FFA analysis for Fig.5 and Fig. 6. L.J.E performed the IHC and tumor burden analysis in Fig. 4 and Fig. 6. S.N.B, L.V, L.G and A.H assisted with dosing the *in vivo* experiments in Fig. 4 and Fig. 6. G.H, W.F.W, J.G, S.B, H.J.H and R.K discovered and developed the series of ACC inhibitors that contain ND-646 and ND-608, conducted the enzyme inhibition and pharmacokinetic characterization of both compounds, and conducted the molecular modeling studies depicted in Fig. 2*b* and Fig. 2*i*.

COMPETING FINANCIAL INTERESTS

J.G. and S.B. are employed by Schrödinger; G.H., W.F.W., H.J.H., and R.K. are employed by Nimbus Therapeutics.

NSCLC inhibited tumor growth. When administered as a single agent or in combination with the standard-of-care drug carboplatin, ND-646 markedly suppressed lung tumor growth in the Kras;Trp53$^{-/-}$ (also known as KRAS p53) and Kras;Stk11$^{-/-}$ (also known as KRAS Lkb1) mouse models of NSCLC. These findings demonstrate that ACC mediates a metabolic liability of NSCLC and that ACC inhibition by ND-646 is detrimental to NSCLC growth, supporting further examination of the use of ACC inhibitors in oncology.

INTRODUCTION

Cancer cells have a fundamental requirement for cellular building blocks including nucleic acids, lipids, and proteins to support continuous proliferation[1]. To accommodate these chronic biosynthetic needs, cancer cells reprogram their metabolism, which has been denoted as one of the hallmarks of cancer[2]. While many studies of tumor metabolism have focused on alterations in glucose and glutamine metabolism, a third well-described metabolic feature long-associated with tumor cells is elevated rates of *de novo* fatty acid synthesis (FASyn)[3–5]. The first committed step of FASyn is mediated by acetyl-CoA carboxylase (ACC), which in mammals is encoded by two related enzymes ACC1 and ACC2, which catalyze the ATP dependent carboxylation of acetyl-CoA to form malonyl-CoA[6]. ACC1 encodes a cytoplasmic isoform that is thought to be the predominant isoform controlling FASyn, whereas ACC2 is tethered to the mitochondrial outer membrane, where localized malonyl-CoA production blocks carnitine palmitoyltransferase-1 (CPT-1) function to prevent fatty acids from entering the mitochondria to undergo fatty acid oxidation (FAOxn)[7]. The multi-domain enzyme fatty acid synthase (FASN) uses malonyl-CoA and acetyl-CoA to catalyze subsequent successive reactions to form fatty acids, predominately palmitate[5]. Subsequent elongation and desaturation reactions produce a milieu of fatty acids that cancer cells rely on for membrane formation, energy storage, and production of signaling molecules[8]. Given that tumor cells rely on FASyn for these needs, and that both ACC1 and FASN mRNAs are upregulated in a number of cancers, FASyn has been postulated to offer a therapeutic window[3–5]. Correspondingly, efforts to target tumor cells bearing elevated rates of lipogenesis have focused on attempts to chemically inhibit either ACC or FASN[5]. However, this strategy has been hampered by the lack of potent and specific compounds that exhibit favorable drug-like properties *in vivo*.

An alternative approach that has been utilized is to mimic a low energy state in tumor cells, which results in an inhibition of FASyn through activation of a low energy checkpoint mediated by the AMP-activated protein kinase (AMPK). AMPK is a serine/threonine kinase that directly inhibits ACC1 and ACC2 via phosphorylation of a highly conserved serine site near their amino-terminus (mouse ACC1 Ser79; human ACC1 Ser117; mouse ACC2 Ser212; human ACC2 Ser222)[9]. Phosphorylation of this serine prevents dimerization of ACC, which is required for activity; and under conditions of cellular energy deprivation, AMPK dominantly inhibits ACC activity[9]. AMPK is activated by the widely used drug metformin, mitochondrial poisons, nucleoside mimetics like the cell-permeable AMP-analog AICAR, and small molecule synthetic AMPK activators; all of which have been shown to possess anti-lipogenic and anti-cancer properties[10–14].

Short interfering RNA (siRNA)-mediated knockdown of ACC1 expression induces apoptosis in prostate[15] and breast[16] cancer cell lines, and chemical inhibition of ACC1 and ACC2 by the macrocyclic myxobacterial natural product soraphen A induces growth arrest and cytotoxicity in prostate cancer cells *in vitro*[17]. However, the clinical use of Soraphen A is precluded by its teratogenicity *in vivo* and poor pharmacokinetic properties and in spite of decades of pharmaceutical efforts to design orally bioavailable small molecule inhibitors, ACC has remained an intractable target[18]. Here we characterize the function of ACC in NSCLC and describe the anticancer effects of ND-646, a small-molecule, orally bioavailable ACC inhibitor derived from our recently described series of allosteric ACC inhibitors[19].

RESULTS

ACC1 activity maintains growth and viability of NSCLC cells

Despite differential subcellular localization and tissue-specific expression of ACC1 and ACC2, several studies suggest significant redundancy between each isoform[14,20,21]. First, to examine the relative expression of ACC1 and ACC2 in NSCLC, we analyzed their mRNA expression levels in eight human NSCLC cell lines (A549, H157, H1355, A427, H23, H460, H358 and H1299) using RNA sequencing (RNAseq). *ACC1* was highly expressed in all eight NSCLC cell lines and was expressed at a substantially higher level than *ACC2*, which had expression levels ranging from low to undetectable (Fig. 1*a*).

To investigate the function of *ACC1* in NSCLC cells we performed CRISPR/Cas9 deletion of *ACC1* in A549 and H157 cells (Fig. 1*b* and Supplementary Fig. 1*a*) and screened clones from each cell line for *ACC1* deletion by immunoblotting. We used an antibody that recognizes both ACC1 and ACC2, as demonstrated by immunoblotting in HEK293T cells transiently expressing each individual isoform (Supplementary Fig. 1*b*). However, *ACC1* deletion in A549 and H157 cells led to complete loss of ACC detection using this antibody, further indicating that ACC2 protein expression is low in these cells (Fig. 1*b*). We isolated two *ACC1*-knockout (*ACC1*-KO) clones from A549 and H157 cells that showed complete loss of ACC1 protein expression and used two clones that had undergone selection for guide RNA (gRNA) transfection and Cas9 expression but lacked deletion of *ACC1*, and hence they expressed wild-type (WT) *ACC1* (Fig. 1*b*). We sequenced *ACC2* in the *ACC1*-null clones to confirm the specificity of the gRNA and found that each *ACC1* null clone retained wild-type alleles of *ACC2*. Stable expression of full-length human wild-type *ACC1* cDNA in an *ACC1*-knockout clone (*ACC1*-KO#1 + *ACC1*) led to similar levels of ACC1 expression as the endogenous ACC1 protein (Fig. 1*b*).

Growth and survival of the ACC1-KO clones were only possible by the exogenous addition of the fatty acid palmitate to the medium, suggesting that FASyn was impaired after *ACC1* deletion. We therefore generated clones that were grown in the presence of exogenous palmitate. To assess the impact of *ACC1* deletion on FASyn we performed metabolic labeling in A549 and H157 clones with [U- $^{13}C_6$]glucose for 24hrs to measure carbon incorporation into newly synthesized fatty acids (FAs). *ACC1* deletion led to a complete loss of FASyn in A549 and H157 cells and we did not detect any newly synthesized palmitate, stearate or oleate in ACC1 null clones; stable ACC1 expression led to restoration of FASyn (Fig. 1*c*). Therefore, ACC1 activity is required for FASyn in these NSCLC cells, and

endogenous ACC2 is unable to compensate for the loss of ACC1 in these cells. However, we found that ACC2 overexpression in 293T *ACC1*-KO cells led to restoration of FASyn, similar to that seen with ACC1 overexpression, suggesting that ACC2 expression levels may dictate the ability of ACC2 to compensate for loss of ACC1 (Supplementary Fig. 1*c*).

To quantitate the impact of ACC1 deletion on proliferation we analyzed cellular growth of WT and *ACC1*-KO A549 and H157 clones that had been grown in palmitate and then plated into media containing either regular fetal bovine serum (FBS) or delipidated FBS in the presence or absence of exogenous palmitate. *ACC1* deletion led to a significant decrease in cellular growth compared to WT controls in medium containing regular FBS that was even more pronounced in delipidated FBS but completely rescued by exogenous palmitate addition or stable ACC1 expression (Fig. 1*d*, Supplementary Fig. 1*d*). We generated two *ACC2*-KO A549 clones, identified by genomic *ACC2* DNA sequencing, and found that *ACC2* deletion had no effect on cellular proliferation (Supplementary Fig. 1*e*). We also performed analogous CRISPR/Cas9 studies in a mouse $Kras^{G12D/+,}$ $p53^{-/-}$ NSCLC cell line (634T)[22] and found that *Acc1* deletion led to a proliferation defect and that *Acc2* deletion had no impact (Supplementary Fig.1*f, g, h*).

Cellular viability was significantly decreased after *ACC1* deletion in A549 and H157 clones (Fig. 1*e*), and we found that *ACC1*-KO clones had increased levels of caspase-cleaved poly(ADP-ribose) polymerase 1 (PARP1) in the absence of palmitate (Fig. 1*f*). Additionally, *ACC1*-KO clones expressed increased levels of C/EBP-homologous protein (CHOP), a transcription factor that regulates the unfolded protein response (UPR) and expression of pro-apoptotic genes in response to ER stress[23], consistent with previous observations with FASN inhibition in cancer cells[24]. Induction of cleaved PARP1 and expression of CHOP in *ACC1*-KO cells was rescued by addition of exogenous palmitate or stable expression of *ACC1* cDNA (Fig. 1*f*).

Finally, to determine the effect of genetic *ACC1* deletion on tumor growth we injected two million WT and *ACC1*-KO tumor cells subcutaneously into the hind flanks of nude mice and performed bioluminescence imaging (BLI) for 42 days (A549) or 49 days (H157) (Fig. 1*g*). WT clones displayed a 65–90 fold increase in bioluminescence during this period, compared to *ACC1*-KO clones which either remained static or had a reduction in bioluminescence, suggesting a decrease in viability over time (Fig. 1*h*). WT clones developed larger more vascularized tumors compared to *ACC1*-KO clones and had significantly increased tumor weights (Fig.1*i*). Importantly, stable ACC1 restoration rescued tumor growth of H157 *ACC1*-KO tumors (Fig.1*h*, *i*). Taken together, these data demonstrate the requirement for ACC1 activity to promote FASyn that is needed for growth and survival of NSCLC *in vitro* and *in vivo*.

ND-646, an allosteric inhibitor of acetyl-CoA carboxylase—We recently described development of a series of allosteric ACC inhibitors, as exemplified by the highly liver-selective compound ND-630, which was designed for the treatment of fatty liver diseases, including non-alcoholic steatohepatitis (NASH)[19]. In order to determine whether pharmacological inhibition of ACC is therapeutic for NSCLC we selected ND-646 from this series because of its broad tissue distribution. ND-646 (Fig. 2*a*), interacts with several

residues within the dimerization site of the biotin carboxylase (BC) domain of ACC[19], including Arg172 in ACC1 and Arg277 in ACC2, which are the same residues with which the AMPK-phosphorylated ACC serine peptides interact[25] (Fig. 2*b*). ND-646 inhibits both ACC1 and ACC2 and therefore precludes the ability of ACC2 to compensate for ACC1 inhibition. Analogously to Soraphen A[26,27] and ND-630[19], ND-646 binding to the BC domain of ACC disrupts enzyme dimerization and inhibits enzymatic activity. ND-646 inhibited dimerization of recombinant human ACC2 BC domain (hACC2-BC) under native conditions; hACC2-BC migrates as a dimer in its absence and a monomer in its presence (Supplementary Fig. 2*a*). In cell free systems, ND-646 inhibited enzymatic activity of recombinant human ACC1 (hACC1) with an IC_{50} of 3.5 nM and recombinant human ACC2 (hACC2) with an IC_{50} of 4.1 nM (Supplementary Fig. 2*b*,*c*). Pharmacokinetic analysis of ND-646 in male CD1 mice, a strain commonly used for nonclinical drug development, demonstrated a favorable drug-like profile of ND-646 (Supplementary Fig. 2*d*). For all subsequent analyses, we also utilized ND-608, a less active enantiomer of a closely related analog of ND-646 (hACC1 IC_{50} = 4,790 nM; hACC2 IC_{50} = 6,540 nM) as a negative control.

AMPK phosphorylation sites in ACC—a biomarker for ND-646—ND-646 interacts within the dimerization site of the BC domain of ACC, specifically binding to Arg172 in human ACC1 ($hACC1^{R172}$) and Arg277 in human ACC2 ($hACC2^{R277}$) (Fig. 2*b*), which is the same residue that the conserved AMPK-phosphorylated serines (p-Ser) in ACC1 and ACC2 bind to inhibit ACC activity[25,28]. AMPK phosphorylation of these serines in the A-domain tail of ACC1 and ACC2 induces a conformational change of the tail to promote binding of P-Ser to Arg, which inhibits BC domain dimerization and enzymatic activity of ACC [25], analogous to effects of ND-646, suggesting that ND-646 and AMPK inhibit ACC via the same mechanism. Because ND-646 and P-Ser bind to the same Arg, and ND-646 has a higher affinity for binding, ND-646 should prevent P-Ser from binding to this Arg. Using a phosphopeptide specific antibody that recognizes the aforementioned conserved AMPK phosphorylation sites in mouse and human ACC1 and ACC2, herein referred to collectively as “P-ACC”, we found that ND-646 treatment of A549 cells inhibited our ability to detect P-ACC at these AMPK phosphorylation sites (Fig. 2*c*). ND-646 treatment led to a complete loss of P-ACC detection in A549 cells without affecting total ACC protein levels at 24hrs. These results were also recapitulated *in vivo* in livers and autochthonous ($Kras^{G12D/+}$; $p53^{-/-}$) lung tumors of mice dosed orally with a single dose of 50 mg/kg ND-646 (Fig. 2*d, e*). To explain how ND-646 inhibits P-ACC detection we tested several hypotheses. ND-646 did not prevent the ability of AMPK to phosphorylate Ser^{222} in the A-domain tail of recombinant hACC2-BC, despite inhibiting BC domain dimerization (Supplemental Fig. 2e). Additionally, ND-646 had no impact on the ability of AMPK to phosphorylate other direct substrates such as Raptor, demonstrating that ND-646 does not inhibit AMPK activity (Supplementary Fig. 2*f*). Next, we reasoned that ND-646 might promote dephosphorylation of P-Ser, potentially explaining why ND-646 inhibits P-ACC detection. We found that co-treatment of A549 cells with ND-646 and the phosphatase inhibitor Calyculin-A completely restored P-ACC detection (Fig. 2*f*). Furthermore, mutation of the Arg172 binding site in human ACC1 to an alanine ($hACC1^{R172A}$), which should prevent P-Ser from binding Arg, analogous to ND-646 binding, led to over-expression of total ACC protein levels but an

inability to detect P-ACC in *ACC1*-KO HEK293T cells (Fig. 2*g*). Calyculin A treatment completely restored P-ACC detection in hACC1^{R172A} expressing cells, suggesting that the un-bound P-Ser peptide in hACC1^{R172A} is constitutively de-phosphorylated (Fig. 2*g*). Additionally, the analogous mutation in hACC2 (hACC2^{R277A}) did not affect the ability of AMPK to phosphorylate hACC2-BC at Ser222 *in vitro* (Supplementary Fig. 2*g*). Taken together, these data suggest that ND-646 binding to the BC domain of ACC promotes its constitutive dephosphorylation by preventing the ability of the AMPK-phosphorylated p-Ser peptide to bind arginine, such that the p-Ser peptide is no longer protected from dephosphorylation. Notably, although dephosphorylation of ACC normally activates the enzyme, in the presence of ND-646, ACC activity remains inhibited, as ACC is unable to dimerize. These results support the mechanistic hypothesis that ND-646 inhibition of ACC activity mimics the physiological regulation of ACC function by AMPK. By modeling the crystal structure of ND-646 bound to hACC2-BC with prior crystal structures of the AMPK phosphorylation site[25], we could visualize the effects of ND-646 binding to ACC that promote its inhibition and dephosphorylation (Fig. 2*h*).

Finally, to determine whether P-ACC status could be used to complement pharmacokinetic analysis of drug exposure *in vivo,* we treated athymic nude mice bearing A549 subcutaneous tumors with a single oral dose of 25 mg/kg ND-646 and measured the levels of ND-646 in tumor tissue and immunoblotted for P-ACC at defined time points of 1 hr. and 8 hr. post dosing. Tumor exposure of ND-646 was high (~15 μM) at 1 hr post dosing which correlated with complete loss of P-ACC detection (Supplementary Figs. 2*h, i*). However, levels of ND-646 in tumors were significantly lower (~0.9 μM) 8 h after a single dose of ND-646, consistent with the short half-life of ND-646 in mice and the ability to detect p-ACC at this time point. These data demonstrate that the P-ACC biomarker correlates well with absolute levels of ND-646 exposure in tumors and suggest that multiple daily doses of ND-646 are optimal for ACC inhibition *in vivo*.

ND-646 inhibits FASyn in NSCLC cells in vitro—Given the pivotal role of ACC1 in regulating *de novo* FASyn, we performed metabolic labeling with [U- $^{13}C_6$]glucose in ND-646 treated A549 cells to measure FASyn (Fig. 3*a*). Analogous to genetic deletion of *ACC1* in A549 and H157 cells, ACC inhibition by ND-646 significantly inhibited the percentage of newly synthesized palmitate (C16:0), demonstrating that ND-646 promotes a near-complete shut down of *de novo* FASyn (Fig. 3*a*). Consistent with this, ND-646 treatment led to loss of Oil-Red-O staining of neutral lipids in A549 cells and a 90% decrease in total fatty acid content within 72 hrs (Fig. 3*b*). Quantitation of individual fatty acids revealed a marked reduction in the pools of a number of fatty acids, including the predominant saturated fatty acids palmitate and stearate upon ND-646 treatment (Fig. 3*c*). ND-646 treatment of A549 cells did not significantly alter cholesterol synthesis, demonstrating that ACC inhibition does not impact acetyl-CoA utilization by non-FASyn pathways (Supplementary Fig. 3*a*). Collectively, these metabolic flux data demonstrate that, analogous to *ACC1* genetic deletion, ACC inhibition by ND-646 results in potent inhibition of FASyn and depletes cellular levels of fatty acids in NSCLC cells.

ND-646 inhibits proliferation and is cytotoxic in NSCLC cells—ND-646 markedly inhibited proliferation (Supplementary Fig. 3*b,c*) and viability (Supplementary Fig. 3*d*) of A549, H157, H1355 and H460 NSCLC cells, demonstrating that ACC inhibition impairs cancer cell growth, consistent with results from the genetic deletion of *ACC1* and consistent with previous studies[16,17]. Additionally, the ability of ND-646 to inhibit proliferation was enhanced when cells were cultured in media containing delipidated FBS (Fig. 3d).

Notably, ND-646 treatment of *ACC1*-KO A549 and H157 clones grown in regular or delipidated FBS did not further affect cellular viability (Fig. 3*e*), and cotreatment of A549 cells with ND-646 and palmitate restored viability and completely rescued the antiproliferative effects of ACC inhibition (Fig. 3*f,g* and Supplementary Fig. 3*e*). Palmitate rescue was also recapitulated in H460 cells (Supplementary Fig. 3*f*) and palmitate had no effect on the ability of ND-646 to inhibit ACC because co-treatment with ND-646 resulted in loss of P-ACC detection, demonstrating that ACC is effectively inhibited in palmitate-rescued cells (Supplementary Fig. 3*g*). These data demonstrate the specificity of ND-646 for ACC inhibition, as palmitate would not be expected to rescue any unexpected off target effects of ND-646.

ND-646 treatment of A549 cells led to induction of apoptosis (Fig. 3*h*) and ER stress (Supplementary Fig. 3*h*). ACC inhibition led to increased phosphorylation of the α-subunit of the eukaryotic translation initiation factor 2 on serine 51 (P-EIF2α^{S51}) and also increased the expression of CHOP. Co-treatment of A549 cells with ND-646 and palmitate completely rescued the effects of ND-646 on ER stress and apoptosis (Fig. 3*i*). Taken together, these data suggest that the anti-proliferative effects of ND-646 are due to inhibition of FASyn and depletion of cellular fatty acids

ND-646 inhibits FASyn and tumor growth in NSCLC xenografts—Our pharmacokinetic studies suggested that ND-646 would be more efficacious when delivered at multiple daily doses. Thus, to explore the impact of chronic ND-646 treatment on NSCLC tumor growth and to determine the efficacy of twice-daily dosing, we treated athymic nude mice bearing established A549 subcutaneous tumors orally with either vehicle twice daily (BID), 25 mg/kg ND-646 once daily (QD), 25 mg/kg ND-646 BID or 50 mg/kg ND-646 QD for 31 days (Fig. 4*a*). ND-646 at 25 mg/kg QD was ineffective at inhibiting tumor growth. However, ND-646 administered at 25 mg/kg BID or 50 mg/kg QD significantly inhibited subcutaneous A549 tumor growth (Fig. 4*b, c*). ND-646 was well tolerated throughout the treatment period, with no significant weight loss occurring after chronic ND-646 dosing, suggesting that the maximum tolerated dose (MTD) had not been reached (Supplementary Fig. 4*a*). Mice were sacrificed at 1 hr post final dose and tissues were either prepared for immunohistochemistry (IHC) or immunoblot analysis. Tumors treated with all doses of ND-646 had lost detection of P-ACC at 1 hr, demonstrating effective tumor penetration and acute ACC inhibition by ND-646 (Fig. 4*d* and Supplementary Fig. 4*b*). Notably, only at the doses of ND-646 that led to significant tumor growth inhibition (25 mg/kg BID and 50 mg/kg QD) was significant elevation of P-EIF2α^{S51} expression observed in tumor lysates (Fig. 4*d*), suggesting that P-EIF2α^{S51} may be a therapeutic biomarker reflective of tumor growth inhibition and P-ACC an ACC target engagement biomarker in this setting.

Supporting the anti-neoplastic properties of ND-646 at 25 mg/kg BID and 50 mg/kg QD in this model, tumors had decreased Ki67 staining (Supplementary Fig. 4*b*, *c*).

We were next interested in the impact of ND-646 on lung tumors growing in their native microenvironment in the lung. To determine whether ND-646 functionally inhibits FASyn *in vivo* we administered deuterated water (^2H_2O) to mice harboring A549 lung tumors to quantify deuterium incorporation into newly synthesized fatty acids in tumors, as a measure of FASyn (Fig. 4*e*). ^2H_2O is incorporated into a number of biosynthetic intermediates required for fatty acid production and only labels fatty acids that are newly synthesized[29]. We injected luciferase expressing A549 cells intravenously into SCID/Beige mice to induce lung colonization and lung tumor growth. A549 lung tumors were grown for 42 d, and then mice were given ^2H_2O (Online Methods) and simultaneously treated with either vehicle or ND-646 at 50 mg/kg BID for a period of 7 d (Fig. 4*e*). After 7 days mice were sacrificed and tumors were harvested and analyzed for FASyn. Deuterium enrichment in plasma H_2O was similar between vehicle and ND-646 treated animals and enrichment was sufficient to quantitate FASyn (Supplementary Fig. 4*d*). Next we measured the mass isotopologue distributions of total palmitate and stearate harvested from A549 tumors and calculated fractional fatty acid synthesis (% of the total pool of palmitate/stearate that is synthesized during the labeling period) for each as detailed in the Methods. Approximately 55% of the measured palmitate in vehicle treated A549 lung tumors was newly synthesized during those 7 days, suggesting that A549 tumors are undergoing high rates of *de novo* FASyn (Fig. 4*f*). Moreover, ND-646 treatment led to a significant reduction in the percentage of newly synthesized palmitate and stearate, demonstrating that FASyn is reduced by ND-646 in A549 lung tumors (Fig. 4*f*). While the above analysis calculates the fraction of total fatty acid pools within tumors that is newly synthesized, it does not take into account changes in molar pool sizes of these fatty acids. Thus, to determine maximal FASyn flux rates in tumors (assuming synthesis occurs entirely within the tumor and turnover/oxidation is minimal) we calculated the molar amount of newly synthesized fatty acid per mg of tumor per day of ^2H_2O labeling. While this model assumes that the labeled pool of palmitate and stearate is newly synthesized, it is also possible that deuterium labeled palmitate and stearate are also taken up from plasma and the surrounding microenvironment. Thus, we expressed this synthesis value as a maximal synthesis rate to account for sources outside the tumor. We found that ND-646 led to significant decreases in maximal FASyn rates of palmitate (60% reduction) and stearate (46% reduction) in A549 lung tumors (Fig. 4*f*).

Next, we examined the specific impact of chronic ND-646 treatment on the growth of A549 NSCLC lung tumors. Given that chronic ND-646 treatment was well tolerated at doses used in our earlier studies, we opted to test the preclinical efficacy of ND-646 at 50 mg/kg BID and also a higher dose of 100 mg/kg BID. Additionally, we included carboplatin, which is a standard of care platinum analog utilized in NSCLC treatment, as a separate treatment group for direct comparison. A549 lung tumor growth was monitored for 3 weeks after intravenous injection by bioluminescence imaging (BLI) and then mice were randomized into their treatment groups and dosed chronically for a period of 6 weeks (Fig. 4*g*). ND-646 was tolerated for the duration of the treatment period and we noted a 10% decrease in body weight of mice dosed with ND-646 at 50 mg/kg BID and 100 mg/kg BID compared to vehicle (Supplemental Fig. 4*e*). ND-646 treatment suppressed the growth of A549 lung

tumors at 50 mg/kg BID and 100 mg/kg BID, as compared to vehicle treatment (Fig. 4*h*). The tumors of vehicle treated mice displayed a 60-fold increase in bioluminescence during the treatment period, compared to the tumors of mice treated with 50 mg/kg and 100 mg/kg ND-646 which increased by 33-fold and 23-fold respectively (Supplemental Fig. 4*f-g*). Next, we prepared H&E stained sections of formalin fixed lungs to analyze histopathological changes of A549 lung tumors (Supplemental Fig. 4*h*). ND-646 treatment resulted in an 80% (50 mg/kg BID) and 82% (100 mg/kg BID) reduction in total lung tumor burden, as compared to that in vehicle-treated mice (Fig. 4*i*), which was notably greater than the reduction in total lung tumor burden for carboplatin-treated mice (52%) in this dosing regimen. Morphometric analysis of tumor size revealed that ND-646 treatment resulted in a 47% (50 mg/kg BID) and 43% (100 mg/kg BID) reduction in average tumor size compared to vehicle treatment (Supplemental Fig. 4*i*). Quantitation of BrdU staining on lung sections using advanced image analysis software (InForm-Perkin Elmer) revealed that ND-646 treatment resulted in a 39% (50 mg/kg BID) and 49% (100 mg/kg BID) decrease in the average number of BrdU positive cells within each tumor (Supplemental Fig. 4*j–k*). Additionally, P-ACC IHC confirmed loss of P-ACC detection in ND-646 treated tumors (Supplemental Fig. 4*j*). Taken together, these data demonstrate that ND-646 is detrimental to growth of NSCLC tumors in preclinical lung xenograft models.

ND-646 inhibits tumor FASyn and growth in genetically engineered mouse models—Next we determined whether ND-646 inhibits FASyn in autochthonous lung tumors derived from the *Kras*^{LSLG12D};*Trp53*$^{fl/fl}$;*R26*^{LSLluc} (KP_{luc}) and *Kras*^{LSLG12D};*Stk11*$^{fl/fl}$;*R26*^{LSLluc} (KL_{luc}) genetically engineered mouse models of NSCLC[30]. In these models, adenovirus-mediated Cre recombinase expression (Ad-Cre) in the lung epithelium (via intranasal instillation) induces oncogenic $Kras^{G12D}$ activation, which is coupled to deletion of either Trp53 (which encodes p53) or serine–threonine kinase 11 (Stk11; better known as Lkb1), as well as to expression of luciferase from the Rosa26 locus ($R26^{LSLluc}$) in the same epithelial cell, resulting in lung tumor formation that can be monitored longitudinally by BLI. We initiated lung tumorigenesis in KP_{luc} and KL_{luc} mice and allowed lung tumors to form for 56 d; we then simultaneously administered ^2H_2O and either vehicle BID or ND-646 at 50 mg/kg BID to mice for a period of 7 d (Online Methods). After 7 d, the mice were euthanized, and the lung tumors were harvested for analysis of FASyn (Fig. 5*a*). Additionally, we harvested plasma to determine the effects of ND-646 on circulating plasma fatty acid levels. Deuterium enrichment analysis of plasma H_2O demonstrated similar enrichment between treatment groups and sufficient enrichment for FASyn analysis (Supplementary Fig. 5*a*). Similar to that observed with A549 lung tumors, fractional synthesis of palmitate in lung tumors from vehicle-treated KP_{luc} and KL_{luc} mice was high, demonstrating that KP_{luc} and KL_{luc} lung tumors are undergoing high rates of *de novo* FASyn (Supplementary Fig. 5*b*). Consistent with decreased fractional synthesis, ND-646 treatment of the mice led to a significant reduction in the maximal rate of palmitate and stearate synthesis in KP_{luc} and KL_{luc} lung tumors (Fig. 5*b*) and also a significant reduction in the levels of total fatty acids (Supplementary Fig. 5*c,d*) and free fatty acids (FFAs) (Fig. 5*c,d* and Supplementary Fig. 5*e*) in the tumors. Finally, ND-646 treatment also significantly reduced the levels of a number of saturated and unsaturated FFAs in the plasma of KP_{luc} and KL_{luc} mice (Fig. 5*e*, *f* and Supplementary Fig. 5*f*).

Finally, we examined the effects of chronic ND-646 dosing on lung tumor growth in these mouse models. We induced lung tumors in KP_{luc} and KL_{luc} mice, let tumors develop for 35 days, and then randomized mice into treatment groups which consisted of either vehicle BID, ND-646 50 mg/kg or 100 mg/kg BID, carboplatin 25 mg/kg every 3 days, or a combination therapy of ND-646 50 mg/kg BID + carboplatin (Fig. 6*a*). Mice were dosed chronically for a period of 6 weeks and monitored, by BLI, for lung tumor growth and response to therapy. We noted a 10% decrease in body weight in KP_{luc} and KL_{luc} mice treated chronically with ND-646, however body weights were maintained at that reduced level throughout the treatment period (Supplementary Fig. 6*a*). A small subset of KP_{luc} and KL_{luc} mice that were dosed with ND-646 at 100 mg/kg BID developed a mild squinty eye phenotype starting after 4 weeks of treatment. We detected a reduction in lung tumor bioluminescence (photon flux) in KP_{luc} and KL_{luc} mice that were dosed with ND-646, relative to that in vehicle-treated mice (Fig. 6*b,c* and Supplementary Fig. 6*b*). Notably, BLI revealed that carboplatin treatment elicited a superior antitumor response in KL_{luc} mice than in KP_{luc} mice; however, treatment with the combination of ND-646 + carboplatin led to an improved response, as compared to monotherapy, in both models (Fig. 6*b,c*). Treatment with the combination of ND-646 + carboplatin led to a larger decrease in body weight than monotherapy with either drug; however, body weights were maintained at that reduced level for the duration of the treatment period (Supplementary Fig. 6*a*). To assess the effects of ND-646 on lung tumorigenesis at the histological level, we prepared H&E-stained lung sections from every mouse in each treatment group (Fig. 6*d,e*). ND-646 treatment led to a significant reduction in total tumor burden, as compared to that by vehicle treatment (Fig. 6*f*). However, whereas the average tumor size was significantly reduced after ND-646 treatment in KP_{luc} tumors, the reduction in KL_{luc} tumors was much more modest (Fig. 6*g*), demonstrating that, as a single agent, ND-646 has a greater effect on tumor size in tumors from KP_{luc} mice than in tumors from KL_{luc} mice. By binning KP_{luc} and KL_{luc} lung tumors into six size ranges we found that ND-646 suppressed the outgrowth of large tumors in KP_{luc} mice, an effect that was not apparent in KL_{luc} mice, which lacked large tumors in general (Fig. 6*h*), demonstrating that ACC inhibition prevents the outgrowth of large KP_{luc} tumors. Of note, carboplatin treatment led to a reduction in total tumor burden in both KL_{luc} and KP_{luc} mice, although it was less effective than ND-646 treatment in any of the conditions tested, except against KL_{luc} tumors (Supplementary Fig. 6*c*). Carboplatin treatment induced nuclear p53 accumulation in KL_{luc} tumors, suggesting that the enhanced efficacy of the drug observed in KL_{luc} tumors might occur through a p53-dependent mechanism to suppress growth (Supplementary Fig. 6*d*).

Treatment with the combination of ND-646 + carboplatin led to a marked antitumor response in both KP_{luc} and KL_{luc} tumors (Fig. 6*d–g*). BrdU quantitation revealed a significant reduction in BrdU positivity of tumors treated with ND-646 singly or in combination with carboplatin in KP_{luc} and KL_{luc} mice (Fig. 6*i* and Supplementary Fig. 6*e*). As expected, ND-646 also led to loss of P-ACC detection in tumors (Supplementary Fig. 6*e*). Finally, ND-646 treatment resulted in a significant reduction in a number of saturated and unsaturated fatty acids in the liver and plasma after 6 weeks (Supplementary Fig. 6*f,g*).

DISCUSSION

The requirement for FASyn is a potential metabolic liability of tumor growth that might be exploited for cancer therapy[5]. Our deuterium labeling supports a model in which lung tumors are undergoing high rates of *de novo* FASyn and the present study is the first to show that pharmacological inhibition of ACC, the rate-limiting enzyme required for *de novo* FASyn, results in robust inhibition of tumor growth in biologically relevant models of NSCLC. Thus, this work supports a critical role of ACC to maintain *de novo* FASyn in order to support lung tumor growth. In contrast, a prior study suggested a tumor suppressor function for ACC in some contexts[31]; however the majority of previous studies support a role for ACC in promoting tumor growth and survival[15–17,32]. Here we found that CRISPR/Cas9 deletion of ACC1 in human NSCLC cells led to complete loss of FASyn accompanied by loss of proliferation, viability, and tumorigenic potential. Systemic inhibition of ACC via the broadly distributed, orally bioavailable inhibitor ND-646 blocked tumor growth and suppressed FASyn in xenograft and genetically engineered autochthonous lung tumors.

Future studies are needed to obtain a deeper understanding of the extent to which distinct oncogenic lesions and other genetic factors modulate sensitivity to ACC inhibitors. In addition, while increased FAOxn itself has been implicated as a metabolic liability in oncology[33], the effects of simultaneous inhibition of FASyn and activation of FAOxn has not been studied as a therapeutic strategy for cancer therapy. Given that ND-646 is an allosteric inhibitor of ACC1 and ACC2, ND-646 by itself would be expected to inhibit FASyn and promote FAOxn, however the tumor cell lines used in our study express little to no endogenous ACC2. Studies examining the effect of ND-646 in tumor cells expressing high levels of both ACC isoforms will contribute to our understanding of the role that ACC2 plays in tumorigenesis. In this context, the ability of ND-646 to prevent the relative redundancy observed between isoforms will be an important feature.

Chronic ND-646 treatment of mice was generally well tolerated in our study. The mild squinty eye phenotype we observed occurred in only a small subset of mice at the highest dose of ND-646 after 4 weeks of chronic dosing. Given the ability of ND-646 to inhibit FASyn in a number of tissues, including lowering plasma levels of fatty acids that might contribute to the antitumor effects of ND-646, ACC inhibition may also favorably affect the morbidity and mortality associated with a number of metabolic diseases, including diabetes, obesity and fatty liver disease[19]. Given the unique mechanism of action of our ACC inhibitors, the P-ACC antibody biomarker described in this report may facilitate the additional discovery of potent small molecules interacting in this region of the enzyme and may aid in determining ACC inhibition and therapeutic response in a clinical setting. Future understanding of mechanisms that dictate sensitivity and requirement of most cancer cells for elevated FASyn remains an interesting area for study, as does strategic and rationale design of combination therapies to enhance the efficacy of ACC inhibition. In summary, our data with ND-646 warrant the further evaluation of ACC inhibitors for cancer to define the therapeutic conditions where ACC inhibitors will find maximal clinical utility.

ONLINE METHODS

Preparation of ND-646 and ND-608

ND-646 [1,4-dihydro-1-[(2*R*)-2-(2-methoxyphenyl)-2-[(tetrahydro-2*H*-pyran-4-yl)oxy]ethyl]-a,a,5-trimethyl-6-(2-oxazolyl)-2,4-dioxothieno[2,3-*d*]pyrimidine-3(2*H*)-acetamide], and ND-608 were prepared as previously described [34]. For cell culture studies ND-646 and ND-608 were solubilized in DMSO. For *in vivo* studies, ND-646 was solubilized by vortexing and sonication in a solution containing 0.9% NaCl, 1% Tween 80 and either 0.5% methylcellulose for subcutaneous tumor studies or Captisol (Cydex: 30% wt/vol in 0.9% NaCl) for lung xenograft and genetically engineered mouse model (GEMM) studies. For vehicle treatment, mice received the same solution with the omission of ND-646. For all studies, ND-646 was administered by oral gavage.

^{13}C tracing

^{13}C tracing experiments were performed with glucose and glutamine-free DMEM containing 10% dialyzed FBS, 15 mM [U-$^{13}C_6$]glucose, and 4 mM glutamine. Cholesterol labeling experiments were conducted in glucose and glutamine-free DMEM containing 10% delipidated dialyzed FBS, 50 μmol/L BSA-palmitate, 15 mM [U-$^{13}C_6$]glucose, and 4 mM glutamine.

Metabolite extraction and GC/MS analysis

Polar and non-polar metabolites were extracted using methanol/water/chloroform as previously described [35]. Briefly, at the conclusion of tracer experiment medium was aspirated and cells were washed twice with 0.9% NaCl saline solution. Methanol (-80 °C) and water containing 1μg/well norvaline as internal standard (4 °C) was immediately added to each well and cells were transferred to tube. Chloroform (-20 °C) was added to each tube followed by vortex and separation into aqueous (polar) and inorganic (non-polar) layers by centrifugation. Layers were transferred to new tubes and evaporated to dryness. Derivatization of polar metabolites, fatty acids, and cholesterol has been previously described [35,36]. Briefly, polar metabolites were derivatized to form methoxime–tert-butyldimethylsilyl (TBDMS) derivatives by incubation with 2% methoxylamine hydrochloride dissolved in pyridine at 37 °C for 1 h followed by addition of N-tert-butyldimethylsilyl-N-methyltrifluoroacetamide (MTBSTFA) with 1% tert-butyldimethylchlorosilane (TBDMCS) incubated at 37 °C for 30–60 min. Nonpolar metabolites were saponified to free fatty acids and transesterified to form fatty acid methyl esters by incubation with 2% H_2SO_4 in methanol at 50 °C for 1 hour. Cholesterol samples were prepared by first transesterifying by incubation with 2% H_2SO_4 in methanol at 50 °C for 1 hour followed by derivatization to TMS derivatives by incubation with pyridine at 37 °C for 1 hour followed by addition of N-methyl (trimethylsilyl) trifluoroacetamide (MSTFA) at 37 °C for 30–60 minutes. Derivatized polar and cholesterol samples were analyzed by GC-MS using a DB-35MS column (30 m x 0.25 mm i.d. x 0.25 um) installed in an Agilent 7890B gas chromatograph (GC) interfaced with an Agilent 5977A mass spectrometer (MS). Lipid samples were analyzed by GC-MS using a Select FAME column (100 m x 0.25 mm i.d.) installed in an Aglient 7890A GC interfaced with an Agilent 5975C

MS. Mass isotopomer distributions were determined by integrating metabolite ion fragments and corrected for natural abundance as previously described [37].

Cell culture and cell lines

All cell lines were incubated at 37 °C and were maintained in an atmosphere containing 5% CO_2. A549, H460, H157 and H1355 cells were purchased from the ATCC. Cells were tested for Mycoplasma (Lonza) using manufacturer's conditions and were deemed negative. Cells were grown in Dulbecco's modified Eagles medium (DMEM) plus 10% fetal bovine serum (Hyclone). *ACC1*-KO clones were maintained in 10% FBS + addition of 200 μM palmitate every 3 days. For proliferation assays via cell counts, cells were plated into 24 well plates in triplicate at 2^{E4} cells/well and the following day treated with either DMSO vehicle or ND-608 or ND-646. Cell counts were recorded at days 1, 3, 5 and 7-post treatment. For delipidated media, cells were first seeded in media containing regular 10% FBS and the following day were switched into media containing 20% delipidated FBS (Gemini #900-123) upon treatment. Viability assays were performed using either a WST-1 viability assay (Roche #05015944001) or Cyquant (Life Technologies #C35011) in 96 well culture plates under manufacturers conditions. For quantitation, values from treated cells were divided by values from control treated cells and expressed as percent control. Palmitate (Sigma Aldrich #P5585) rescue experiments were performed in delipidated media by co-treating cells, in 24 well plates, with either ND-608 or ND-646 and 200 μM of palmitate conjugated to BSA. For palmitate-BSA preparation, palmitate was solubilized in 100% Etoh @ 50 mM and combined with 4% fatty acid free BSA (Sigma Aldrich #A8806) in saline at a ratio of 1:4 to make a palmitate concentration of 10 mM. Palmitate-BSA was used at a final concentration of 200 μM.

CRISPR/Cas9 studies

ACC Knockouts were generated using the Cas9 nickase strategy as described[38,39]. Briefly, separate pairs of guide RNAs (gRNA) were designed to target each of the human and mouse *ACC1* and *ACC2* genes (*ACACA, ACACB*, *Acaca, Acacb*), using the online design tool at crispr.mit.edu. Each gRNA duplex was cloned into pX462 vector encoding SpCas9n-2A-puro (Addgene # 48141). A549, H157, 634T and HEK293T cells were transfected with the respective *ACC1* or *ACC2* gRNA pair to generate single knockouts. After puromycin selection, single cell cloning was performed by cell sorting into 96-well plates. Clones were maintained by adding 200 μM palmitate-BSA to the cell culture media every 3–4 days. For *ACC1*, individual clones were screened by western blot for ACC1 protein expression. For *ACC2*, genomic DNA was sequenced to identify null alleles. *ACC1* restoration was performed by infecting H157 *ACC1*-KO clone#1 with lenti-virus expressing full-length human *ACC1* cDNA. Stable integrants were selected and maintained with puromycin.

Mouse studies

All procedures using animals were approved by the Salk Institute Institutional Animal Care and Use Committee (IACUC). *Subcutaneous tumor studies*: For *ACC1*-KO studies, 8 week old athymic female nude mice (J:NU 007850, Jackson Labs) were injected subcutaneously into the hind flanks with 2^{E6} cells of either WT or *ACC1*-KO luciferase expressing clones in a volume of 200 μl and imaged by BLI 20 mins after injection. Mice underwent BLI weekly

for a period of 42 days (A549) and 49 days (H157), then mice were sacrificed and tumors were dissected and weighed. For ND-646 subcutaneous studies, female athymic nude mice were injected subcutaneously into the hind flanks with 5^{E6} A549 cells. Tumor growth was measured daily using digital calipers and volumes were calculated using the formula ½ [L x W] ^{2}. Tumor prevention studies began at 11 days post tumor cell injection. Mice were randomized into their treatment groups based on similar average tumor volumes. The average tumor volume at the initiation of treatment was 40 mm^3. Mice were dosed orally (Per OS) once or twice a day with either a vehicle solution (0.9% NaCl, 1% Tween 80, 0.5% methylcellulose) or ND-646 at either 25 mg/kg or 50 mg/kg (0.9% NaCl, 1% Tween 80, 0.5% methylcellulose). At the end of the study, mice were euthanized 1hr post final dose. *Intravenous lung tumor studies*: 8 week old female SCID/Beige ($Prkdc^{scid}Lyst^{bg-J}$/Crl:Fox Chase#250) were injected i.v with 1^{E6} luciferase expressing H157 or A549 cells for FASyn studies or 2.5^{E5} cells for tumor prevention studies. All mice were imaged via BLI 20 mins after i.v injection. For FASyn studies tumors were grown for 42 days before mice were simultaneously placed on ^2H_2O and treated with either vehicle or ND-646. Mice were dosed bi-daily for 1 week before plasma, tumor was harvested. For tumor prevention studies, mice underwent BLI 21 days post i.v injection and were randomized into their treatment groups based on similar average photon flux (photons/sec) in the region of interest encompassing the thoracic cavity. Mice were monitored for lung tumor growth by BLI weekly. Carboplatin (Sigma) was dissolved in 0.9% saline and administered via i.p injection. Mice were dosed chronically for 6 weeks. At the end of 6 weeks mice were injected with 100 mg/kg of BrdU (Sigma) and sacrificed 4hrs later. Lungs were inflated with 10% formalin, fixed in 10% formalin for 18 hrs and then paraffin embedded for histopathology studies. *Genetically engineered mouse model studies*: 10 week old FVB/n $Kras^{LSLG12D/+;}$ $p53^{fl/fl}$ $R26^{LSL:luc/luc}$ (KP_{luc}) and $Kras^{LSLG12D/+;}$ $LKB1^{fl/fl}$ $R26^{LSL:luc/luc}$ (KL_{luc}) mice have been described previously[30].

For all experiments utilizing KP_{luc} and $KL_{luc,}$ a mixture of female and male mice were used. For FASyn studies, mice were treated intranasally with Ad-Cre and were simultaneously placed on ^2H_2O and treated with either vehicle or ND-646 at 56 d post inhalation. Mice were dosed twice daily for 1 week before plasma and lung tumors were harvested. Five mice were used per treatment, and three tumors per mouse were analyzed. For tumor-prevention studies, mice were treated intranasally with Ad-Cre and imaged bi-weekly using BLI. At 35 d post inhalation, mice underwent BLI and were assigned into their treatment groups based on similar average photon flux (photons/s) in the region of interest encompassing the thoracic cavity. Mice were excluded from future study if they failed to develop bioluminescent tumors at day 35. Mice were dosed chronically for 6 weeks and were subject to procedures identical to those for the i.v. studies mentioned previously. 9–14 mice were used per treatment and were monitored for lung tumor growth by BLI every two weeks. For all BLI, D-Luciferin (150 mg/kg) was administered I.P to mice for 10 mins prior to imaging. For all mouse BID dosing, the time between doses was approximately 8 hrs. Baseline body weights were recorded at the initiation of treatment and were recorded daily throughout the treatment period. Mice were also monitored for potential adverse events and for general health status during the course of the study. Power calculations were not used to determine sample size of mice. Sample size was chosen based on available litter sizes or previously

established studies that sufficiently accounted for variability among animals to determine a pre-clinical effect. For statistical analysis, variances were similar between all treatment groups. *Post hoc analyses from tumor sections.* For A549 lung xenograft and GEMM studies, tumor size per treatment was calculated by measuring each individual tumor size from H&E-stained sections using morphometric analysis in Panoramic viewer software (3D Histech). To quantitate lung tumor area, individual tumor sizes were summed for each mouse from each treatment and the percentage of tumor encompassing total lung area was calculated per mouse per treatment. Total lung area was quantitated using Panoramic viewer software.

Deuterated water (^2H_2O) *in vivo* FASyn studies

Seven days before euthanization, mice were treated with either vehicle or ND-646 and simultaneously placed onto ^2H_2O by i.p. injection with 0.035 mL per g of mouse body weight with 0.9% NaCl ^2H_2O. Drinking water was immediately replaced with 8% ^2H_2O-enriched water and mice remained on ^2H_2O for the entire treatment period. Mice were fasted for 6 h before plasma and tissue collection. Plasma enrichment of ^2H_2O was approximately 5% of body water after 7 days of labeling. ***Plasma ^2H_2O enrichment***: The 2H labeling of water from samples or standards was determined via deuterium acetone exchange[40,41]. 5 μL of sample or standard was reacted with 4 μL of 10N NaOH and 4 μL of a 5% (v/v) solution of acetone in acetonitrile for 24 hours. Acetone was extracted by the addition of 600 μl chloroform and 0.5 g Na2SO4 followed by vigorous mixing. 100 μL of the chloroform was then transferred to a GCMS vial. Acetone was measured using an agilent DB-35MS column (30 m 3 0.25mm i.d. 3 0.25 mm, Agilent J&W Scientific) installed in an Agilent 7890A gas chromatograph (GC) interfaced with an Agilent 5975C mass spectrometer (MS) with the following temperature program: 60 °C initial, increase by 20 °C/min to 100 °C, increase by 50 °C/min to 220 °C, and hold for 1 min. The split ratio was 40:1 with a helium flow of 1 ml/min. Acetone eluted at approximately 1.5min. The mass spectrometer was operated in the electron impact mode (70 eV). The abundance of mass ions 58–64 was quantified and corrected for natural abundance. Up to six deuterium atoms can transfer to acetone depending on ^2H_2O enrichment, thus, mole-percent enrichment was quantified and compared to a ten-point standard curve to quantify plasma ^2H_2O enrichment.

Total fatty acids were extracted from tissues and plasma using a bligh and dyer based methanol/chloroform/water extraction with [U-$^2H_{31}$] C16:0 (d31-C16:0) as an internal standard. Briefly, 500 μL MeOH, 500 μL CHCL3, 200 μL H_2O and 10 μL 10 mM d31-C16:0/ 10 mgs tissue were added to weighed pre-ground tissue. This was vortexed for 10 minutes followed by centrifugation at 10,000 g for 5 minutes. The lower chloroform phase was dried and then derivitised to form fatty acid methyl esters (FAMEs) via addition of 500 μL 2% H2SO4 and incubation at 50 °C for 2 hours. FAMEs were extracted via addition of 100 μL saturated salt solution and 500 μL hexane and these were analyzed using a Select FAME column (100 m x 0.25mm i.d.) installed in an Aglient 7890A GC interfaced with an Agilent 5975C MS. ***Calculations***: The mass isotopomer distributions of each fatty acid was determined and corrected for natural abundance using in-house algorithms adapted from Fernandez (1996)[37]. Calculation of the fraction of newly synthesized fatty acids (FNS) was based on the method described by Lee et al[29] where FNS is described by the following

equation: FNS=ME/(n x p) Where ME is the average number of deuterium atoms incorporated per molecule (ME =1 x m_1 + 2 x m_2 +3 x m_3 ...), p is the deuterium enrichment in water and n is the maximum number of hydrogen atoms from water incorporated per molecule. N was determined using the equation: m2/m1 = ((N – 1)/2) × p/q as described by Lee et al.[42], where q is the fraction of hydrogen atoms and p + q = 1. Fractional synthesis rates (FSRs) were calculated by the following equation: FSR = FNS × (n_{FA}/t), where n_FA represents the molar amount of each fatty acid, and t is the time for which ^2H_2O was administered.

FFA Analysis

Extracted samples were dissolved in 100 μL $CHCl_3$; 15 μL was injected for analysis. LC separation was achieved using a Bio-Bond 5U C4 column (Dikma). The LC solvents were as follows: buffer A, 95:5 H_2O:methanol + 0.03% NH_4OH; buffer B, 60:35:5 isopropanol:methanol:H_2O + 0.03% NH_4OH. A typical LC run consisted of the following for 70 minutes after injection: 0.1 mL/min 100% buffer A for 5 minutes, 0.4 mL/min linear gradient from 20% buffer B to 100% buffer B over 50 min, 0.5 mL/min 100% buffer B for 8 minutes and equilibration with 0.5 mL/min 100% buffer A for 7 minutes. FFA analysis was performed using a Thermo Scientific Q Exactive Plus fitted with a heated electrospray ionization source. The MS source parameters were 4kV spray voltage, with a probe temperature of 437.5°C and capillary temperature of 268.75°C. Full scan MS data was collected with a resolution of 70k, AGC target $1x10^6$, max injection time of 100 ms and scan range 150–2000 m/z. Data-dependent MS (top 5 mode) was acquired with a resolution of 35 k, AGC target 1×10^5, max injection time of 50 ms, isolation window 1 m/z, scan range 200 to 2,000 m/z, stepped normalized collision energy (NCE) of 20, 30 and 40. Extracted ion chromatograms for each FFA was generated using a m/z ± 0.01 mass window around the calculated exact mass (i.e. palmitic acid, calculated exact mass for M-H is 255.2330 and the extracted ion chromatogram was 255.22–255.24). Quantification of the FFAs was performed by measuring the area under the peak and dividing this number by the area under the peak for the $^{13}C_{16}$-palmitic acid. The ratio of FFA/$^{13}C_{16}$- PA was then multiplied by 200 pmol (the concentration of the $^{13}C_{16}$-palmitic acid) and divided by the tumor weight or plasma volume to afford the molar concentration per unit mass or unit volume.

Immunohistochemistry and image analysis

Formalin fixed tumors were transferred into 70% EtoH after 18hrs and paraffin embedded (FFPE) at the Salk Institute Histology Core. 5 μm sections from FFPE tissues were prepared and stained with hematoxylin and eosin. For immunohistochemistry, slides were deparaffinized and rehydrated. Antigen retrieval was performed with citrate buffer (11 minutes at high heat for P-ACC, 30 minutes at high heat for BrdU). Endogenous peroxidase activity was quenched with hydrogen peroxide. Using the ImmPress HRP Ig (Peroxidase) Polymer Detection Kits (Vector Labs), slides were blocked, incubated overnight with primary antibody diluted in blocking buffer, and secondary antibody steps were carried out according to the manufacturer's instructions. Staining was visualized using ImmPACT DAB Peroxidase Substrate (Vector Labs, SK-4105). Slides were counterstained with hematoxylin, dehydrated, and mounted with Cytoseal 60 (Thermo Scientific). Primary antibodies used were specific to the following proteins: p-ACC(Ser79) (Cell Signaling Technology, %11818,

1:400), BrdU (Abcam, %6326, 1:200) and p53 (clone CM5 1:200, Novocastra). Immunostained slides were scanned using a Perkin Elmer Slide Scanner (Panoramic MIDI Digital Slide Scanner). Inform v2.1 image analysis software (Cambridge Research and Instrumentation) was used as a non-biased method to quantitate BrdU and p53 staining. Briefly, for each region analyzed, hematoxylin-stained nuclei were identified by the software and tallied to generate a total cell count per tumor. Nuclei were also analyzed for diaminobenzidine (DAB) staining and were, correspondingly, binned as negative or positive for BrdU, or binned by staining intensity on a 4-bin scale for p53. A ratio between the number of DAB-positive and total nuclei was used to calculate the % of cells staining positive for BrdU or within different staining intensity categories for p53 per tumor. Quantitative analysis was performed on individually cropped tumors from all mice per treatment group for BrdU and a subset of mice for vehicle, carboplatin and ND-646 + carboplatin for p53. For BrdU, the % BrdU positive cells was then determined for each tumor and plotted. For p53, the nuclear staining intensity was plotted for each treatment. For analysis, investigators were blinded to the treatment condition by random assignment of mouse numbers that were naïve to the investigators.

Statistical analyses

Statistical analyses are described in each figure and all were performed using Graph Pad Prism 7. For statistical test selection, distribution fitting and variance testing was determined to justify test selection. The majority of the data had similar variance and all data met the assumptions of the statistical test. For all statistical analyses, significance was accepted at the 95% confidence level.

Supplementary Material

Refer to Web version on PubMed Central for supplementary material.

Acknowledgments

This study was supported by grants to R.J.S. from the National Institutes of Health (R01CA172229, P01CA120964), the Samuel Waxman Cancer Research Foundation, The Leona M. and Harry B. Helmsley Charitable Trust grant #2012-PG- MED002, the NIH to C.M.M. (R01CA188652), and the Department of Defense to C.M.M and R.J.S. (W81-XWH-13-1-01-5). R.U.S. was supported by a postdoctoral fellowship from the American Cancer Society (ACS#124183-PF-13-023-01-CSM). L.J.E. was supported by a T32 postdoctoral training grant to the Salk Institute Cancer Center (5 T32 CA009370) and a postdoctoral fellowship from the American Cancer Society (PF-15-037-01-DMC). S.J.P. was supported by an F31 NIH pre-doctoral training fellowship (F31CA196066-01). M.J.K is supported by a UCSD Medical Scientist Training Program fellowship (2 T32 GM007198). P.S.L was supported by a T32 predoctoral training grant (T32 GM 007240). S.N.B is supported by a T32 postdoctoral training grant to the Salk Institute Cancer Center (T32: 5T32CA009370-33). J.L.V.N is supported by a Damon Runyon Cancer Research Foundation Fellowship (DRG-2219-15). We thank K. McIntyre and the histology core at the Salk Institute, which is also supported in part through the Salk CCSG P30 CA014195 grant, as well as the next-generation sequencing (NGS) core facility at the Salk Institute, which is supported with funding from the NIH–NCI CCSG P30 014195 grant. We also thank the Chapman Foundation, the Glenn Foundation, and the Helmsley Charitable Trust for their assistance, R. Farid for Figure 2*b*, E. Smith for Figure 2*j*, G. Wahl for the p53-specific antibody used in the IHC experiments and P. Hollstein for technical assistance.

References

1. Vander Heiden MG, Cantley LC, Thompson CB. Understanding the Warburg effect: the metabolic requirements of cell proliferation. Science. 2009; 324:1029–1033. [PubMed: 19460998]

2. Hanahan D, Weinberg RA. Hallmarks of cancer: the next generation. Cell. 2011; 144:646–674. [PubMed: 21376230]
3. Kuhajda FP. Fatty-acid synthase and human cancer: new perspectives on its role in tumor biology. Nutrition. 2000; 16:202–208. [PubMed: 10705076]
4. Menendez JA, Lupu R. Fatty acid synthase and the lipogenic phenotype in cancer pathogenesis. Nat Rev Cancer. 2007; 7:763–777. [PubMed: 17882277]
5. Currie E, Schulze A, Zechner R, Walther TC, Farese RV Jr. Cellular fatty acid metabolism and cancer. Cell Metab. 2013; 18:153–161. [PubMed: 23791484]
6. Wakil SJ, Abu-Elheiga LA. Fatty acid metabolism: target for metabolic syndrome. J Lipid Res. 2009; 50(Suppl):S138–143. [PubMed: 19047759]
7. McGarry JD, Leatherman GF, Foster DW. Carnitine palmitoyltransferase I. The site of inhibition of hepatic fatty acid oxidation by malonyl-CoA. The Journal of biological chemistry. 1978; 253:4128–4136. [PubMed: 659409]
8. Zhang F, Du G. Dysregulated lipid metabolism in cancer. World journal of biological chemistry. 2012; 3:167–174. [PubMed: 22937213]
9. Steinberg GR, Kemp BE. AMPK in Health and Disease. Physiol Rev. 2009; 89:1025–1078. [PubMed: 19584320]
10. Fogarty S, Hardie DG. Development of protein kinase activators: AMPK as a target in metabolic disorders and cancer. Biochim Biophys Acta. 2010; 1804:581–591. [PubMed: 19778642]
11. Swinnen JV, et al. Mimicry of a cellular low energy status blocks tumor cell anabolism and suppresses the malignant phenotype. Cancer Res. 2005; 65:2441–2448. [PubMed: 15781660]
12. Zadra G, et al. A novel direct activator of AMPK inhibits prostate cancer growth by blocking lipogenesis. EMBO molecular medicine. 2014; 6:519–538. [PubMed: 24497570]
13. O'Brien AJ, et al. Salicylate activates AMPK and synergizes with metformin to reduce the survival of prostate and lung cancer cells ex vivo through inhibition of de novo lipogenesis. The Biochemical journal. 2015
14. Fullerton MD, et al. Single phosphorylation sites in Acc1 and Acc2 regulate lipid homeostasis and the insulin-sensitizing effects of metformin. Nature medicine. 2013; 19:1649–1654.
15. Brusselmans K, De Schrijver E, Verhoeven G, Swinnen JV. RNA interference-mediated silencing of the acetyl-CoA-carboxylase-alpha gene induces growth inhibition and apoptosis of prostate cancer cells. Cancer research. 2005; 65:6719–6725. [PubMed: 16061653]
16. Chajes V, Cambot M, Moreau K, Lenoir GM, Joulin V. Acetyl-CoA carboxylase alpha is essential to breast cancer cell survival. Cancer research. 2006; 66:5287–5294. [PubMed: 16707454]
17. Beckers A, et al. Chemical inhibition of acetyl-CoA carboxylase induces growth arrest and cytotoxicity selectively in cancer cells. Cancer research. 2007; 67:8180–8187. [PubMed: 17804731]
18. Tong L, Harwood HJ Jr. Acetyl-coenzyme A carboxylases: versatile targets for drug discovery. J Cell Biochem. 2006; 99:1476–1488. [PubMed: 16983687]
19. Harriman G, et al. Acetyl-CoA carboxylase inhibition by ND-630 reduces hepatic steatosis, improves insulin sensitivity, and modulates dyslipidemia in rats. Proc Natl Acad Sci U S A. 2016; 113:E1796–1805. [PubMed: 26976583]
20. Savage DB, et al. Reversal of diet-induced hepatic steatosis and hepatic insulin resistance by antisense oligonucleotide inhibitors of acetyl-CoA carboxylases 1 and 2. J Clin Invest. 2006; 116:817–824. [PubMed: 16485039]
21. Harada N, et al. Hepatic de novo lipogenesis is present in liver-specific ACC1-deficient mice. Molecular and cellular biology. 2007; 27:1881–1888. [PubMed: 17210641]
22. Gandhi L, et al. Sunitinib prolongs survival in genetically engineered mouse models of multistep lung carcinogenesis. Cancer Prev Res (Phila). 2009; 2:330–337. [PubMed: 19336729]
23. Zinszner H, et al. CHOP is implicated in programmed cell death in response to impaired function of the endoplasmic reticulum. Genes Dev. 1998; 12:982–995. [PubMed: 9531536]
24. Little JL, Wheeler FB, Fels DR, Koumenis C, Kridel SJ. Inhibition of fatty acid synthase induces endoplasmic reticulum stress in tumor cells. Cancer research. 2007; 67:1262–1269. [PubMed: 17283163]

25. Cho YS, et al. Molecular mechanism for the regulation of human ACC2 through phosphorylation by AMPK. Biochemical and biophysical research communications. 2010; 391:187–192. [PubMed: 19900410]
26. Shen Y, Volrath SL, Weatherly SC, Elich TD, Tong L. A mechanism for the potent inhibition of eukaryotic acetyl–coenzyme A carboxylase by soraphen A, a macrocyclic polyketide natural product. Mol Cell. 2004; 16:881–891. [PubMed: 15610732]
27. Wei J, Tong L. Crystal structure of the 500-kDa yeast acetyl-CoA carboxylase holoenzyme dimer. Nature. 2015; 526:723–727. [PubMed: 26458104]
28. Munday MR, Campbell DG, Carling D, Hardie DG. Identification by amino acid sequencing of three major regulatory phosphorylation sites on rat acetyl-CoA carboxylase. European journal of biochemistry / FEBS. 1988; 175:331–338.
29. Lee WN, Bassilian S, Lim S, Boros LG. Loss of regulation of lipogenesis in the Zucker diabetic (ZDF) rat. Am J Physiol Endocrinol Metab. 2000; 279:E425–432. [PubMed: 10913044]
30. Shackelford DB, et al. LKB1 inactivation dictates therapeutic response of non-small cell lung cancer to the metabolism drug phenformin. Cancer Cell. 2013; 23:143–158. [PubMed: 23352126]
31. Jeon SM, Chandel NS, Hay N. AMPK regulates NADPH homeostasis to promote tumour cell survival during energy stress. Nature. 2012; 485:661–665. [PubMed: 22660331]
32. Wang C, et al. Acetyl-CoA carboxylase-alpha inhibitor TOFA induces human cancer cell apoptosis. Biochemical and biophysical research communications. 2009; 385:302–306. [PubMed: 19450551]
33. Camarda R, et al. Inhibition of fatty acid oxidation as a therapy for MYC-overexpressing triple-negative breast cancer. Nature medicine. 2016; 22:427–432.
34. Harriman, GC.; Masse, CE.; Harwood, HJ., Jr; Baht, S.; Greenwood, JR. ACC inhibitors and uses thereof. US patent 8,969,557. 2015.
35. Metallo CM, et al. Reductive glutamine metabolism by IDH1 mediates lipogenesis under hypoxia. Nature. 2011; 481:380–384. [PubMed: 22101433]
36. Lewis CA, et al. Tracing compartmentalized NADPH metabolism in the cytosol and mitochondria of mammalian cells. Mol Cell. 2014; 55:253–263. [PubMed: 24882210]
37. Fernandez CA, Des Rosiers C, Previs SF, David F, Brunengraber H. Correction of 13C mass isotopomer distributions for natural stable isotope abundance. Journal of mass spectrometry : JMS. 1996; 31:255–262. [PubMed: 8799277]
38. Ran FA, et al. Genome engineering using the CRISPR-Cas9 system. Nat Protoc. 2013; 8:2281–2308. [PubMed: 24157548]
39. Ran FA, et al. Double nicking by RNA-guided CRISPR Cas9 for enhanced genome editing specificity. Cell. 2013; 154:1380–1389. [PubMed: 23992846]
40. McCabe DC, Rajakumar B, Marshall P, Smith IW, Ravishankara AR. The relaxation of OH (v=1) and OD (v=1) by H2O and D2O at temperatures from 251 to 390 K. Physical chemistry chemical physics : PCCP. 2006; 8:4563–4574. [PubMed: 17047754]
41. Yang D, et al. Assay of low deuterium enrichment of water by isotopic exchange with [U-13C3]acetone and gas chromatography-mass spectrometry. Anal Biochem. 1998; 258:315–321. [PubMed: 9570847]
42. Lee WN, et al. In vivo measurement of fatty acids and cholesterol synthesis using D2O and mass isotopomer analysis. Am J Physiol. 1994; 266:E699–708. [PubMed: 8203508]

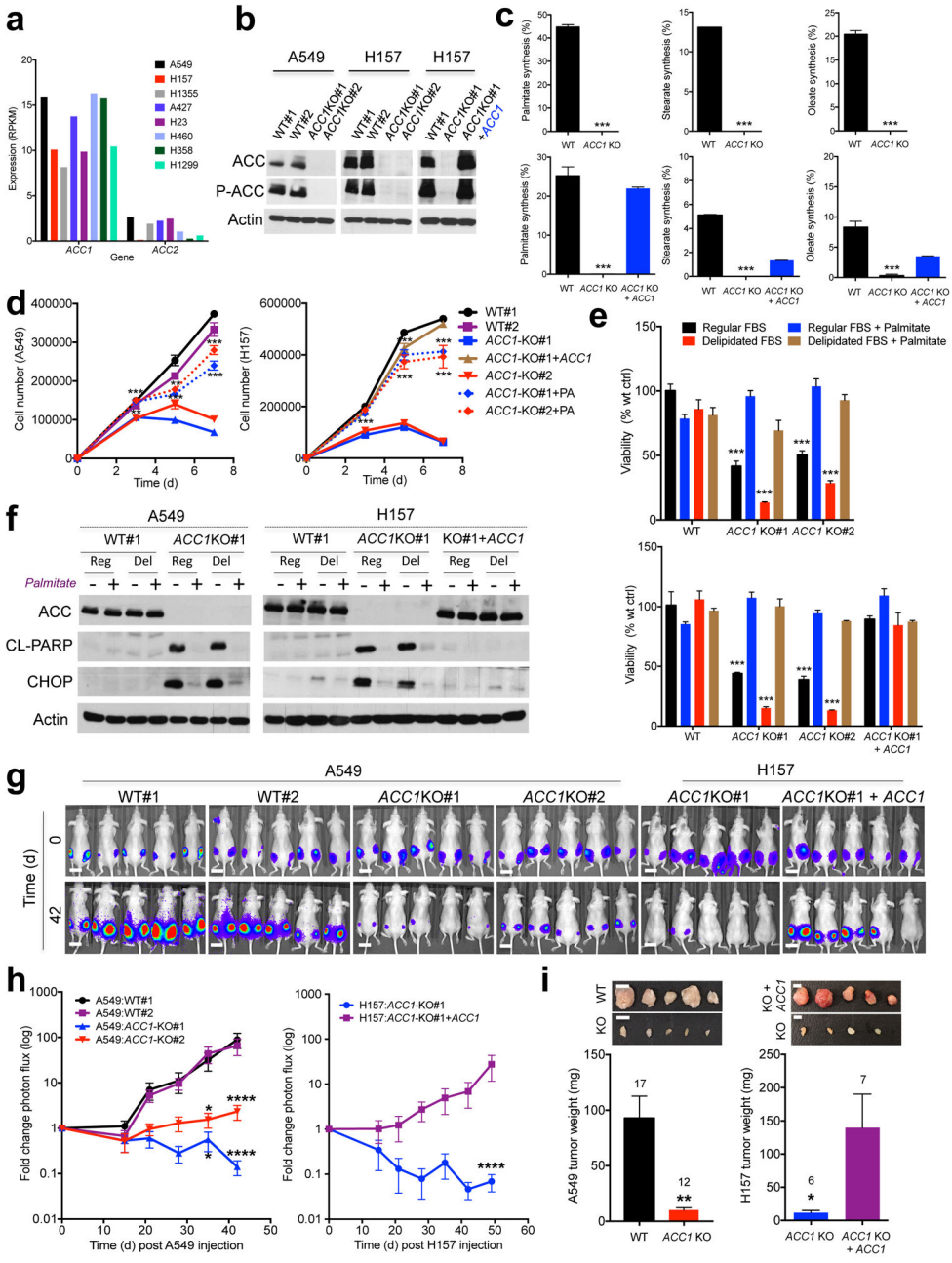

Figure 1. Acetyl-CoA Carboxylase 1 (ACC1) is required for FASyn to support viability of non-small cell lung cancer cells *in vitro* and *in vivo*

(**a**) *ACC1* and *ACC2* mRNA expression in eight human NSCLC cell lines.

(**b**) CRISPR/Cas9 deletion of *ACC1* in A549 and H157 NSCLC cells. Western blot shows ACC detection from one of three separate experiments.

(**c**) Palmitate (left), stearate (middle) or oleate (right) synthesis in [U-$^{13}C_6$]glucose labeled A549 clones (top) or H157 clones (bottom).

(**d**) Cellular growth of A549 and H157 WT and *ACC1*-KO clones in medium containing regular FBS ± 200 μM exogenous palmitate (PA).

(**e**) Viability of WT and *ACC1*-KO clones (A549: top, H157: bottom) after 7 days.

(**f**) Cleaved PARP and CHOP expression in WT and *ACC1*-KO clones after 5 days of growth.

(**g**) Bioluminescence overlay images of subcutaneous growth of WT and *ACC1*-KO clones in nude mice (n=5 per clone). Day 42 images normalized to Day 0. Scale bar =1 cm

(**h**) Tumor growth of WT and *ACC1*-KO clones, represented as logarithmic fold change in photon flux during each imaging time-point relative to Day 0 (n= 10 tumors per clone).

(**i**) Average weight of all tumors from A549 (left) and H157 (right) clones. Number in graph represents total number of tumors per genotype. Inset images are representative of dissected tumors. Scale bar =1 cm.

For (**c–e**) triplicate values were recorded and data are shown from one of least two separate experiments. All values are expressed as means ± s.e.m. * P<0.05 ** P<0.01 *** P<0.001 **** P< 0.0001 relative to WT (**c**, **e**, **h–i**-left) or relative to *ACC1*-KO (**d**, **h–i**-right) determined by ANOVA (**d**, **e**, **h**) with Tukeys method for multiple comparison or two sided student t test (**c**, **i**).

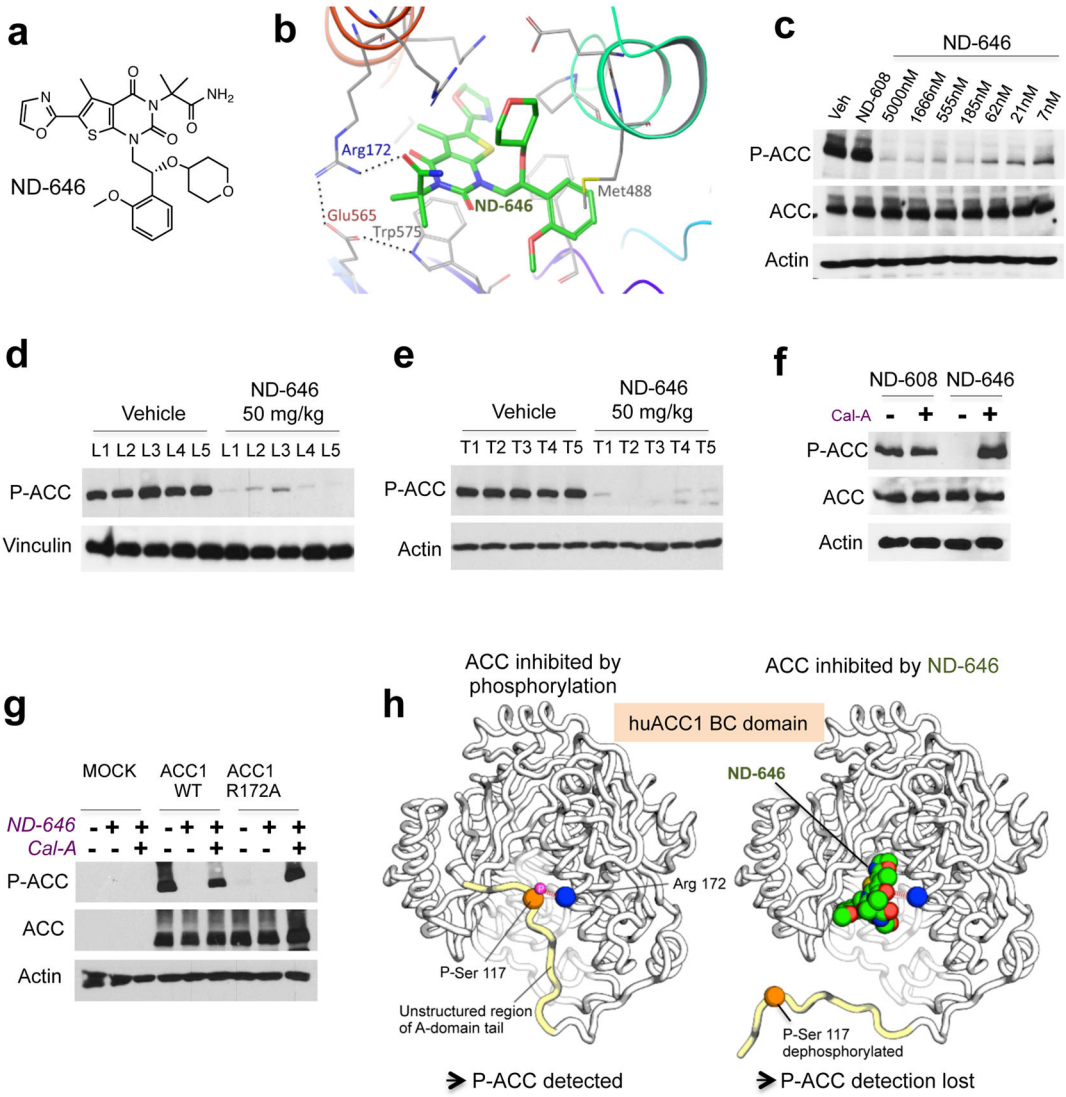

Figure 2. Properties of ND-646, a small molecule allosteric inhibitor of ACC. AMPK phosphorylation sites can be used as a biomarker to monitor ACC engagement by ND-646

(**a**) Chemical structure of ND-646.

(**b**) Model of ND-646 bound to the BC domain of human ACC1. Image depicts a docked pose of ND-646 and ACC1 derived from co-crystal structures of ND-646 complexed with huACC2.

(**c**) P-ACC detection in A549 cells treated for 24 hrs with 5000 nM ND-608 or a dose response of ND-646.

(**d**) P-ACC detection in livers of FVB/n mice and (**f**) $Kras^{G12D/+}$; $p53^{-/}$ lung tumors in mice treated orally with a single dose of vehicle or 50 mg/kg ND-646 for 3 hrs. Numbers represent individual samples from separate mice (n=5 per treatment).

(**f**) P-ACC detection in A549 cells co-treated with either 500 nM ND-608 or ND-646 ± Calyculin A (Cal-A) for 1 hr.

(**g**) P-ACC detection in *ACC1*-KO HEK293 cells transiently expressing Mock, ACC1 wild-type or ACC1 phosphopeptide binding mutant ($ACC1^{R172A}$). Cells were treated with 500 nM ND-646 ± Cal-A.

(**h**) Model describing the mechanism of ACC inhibition by ND-646 and the P-ACC biomarker. Identical effects occur in ACC2-BC at the conserved residues.

For (**c**–**g**) data are representative from one of at least two separate experiments.

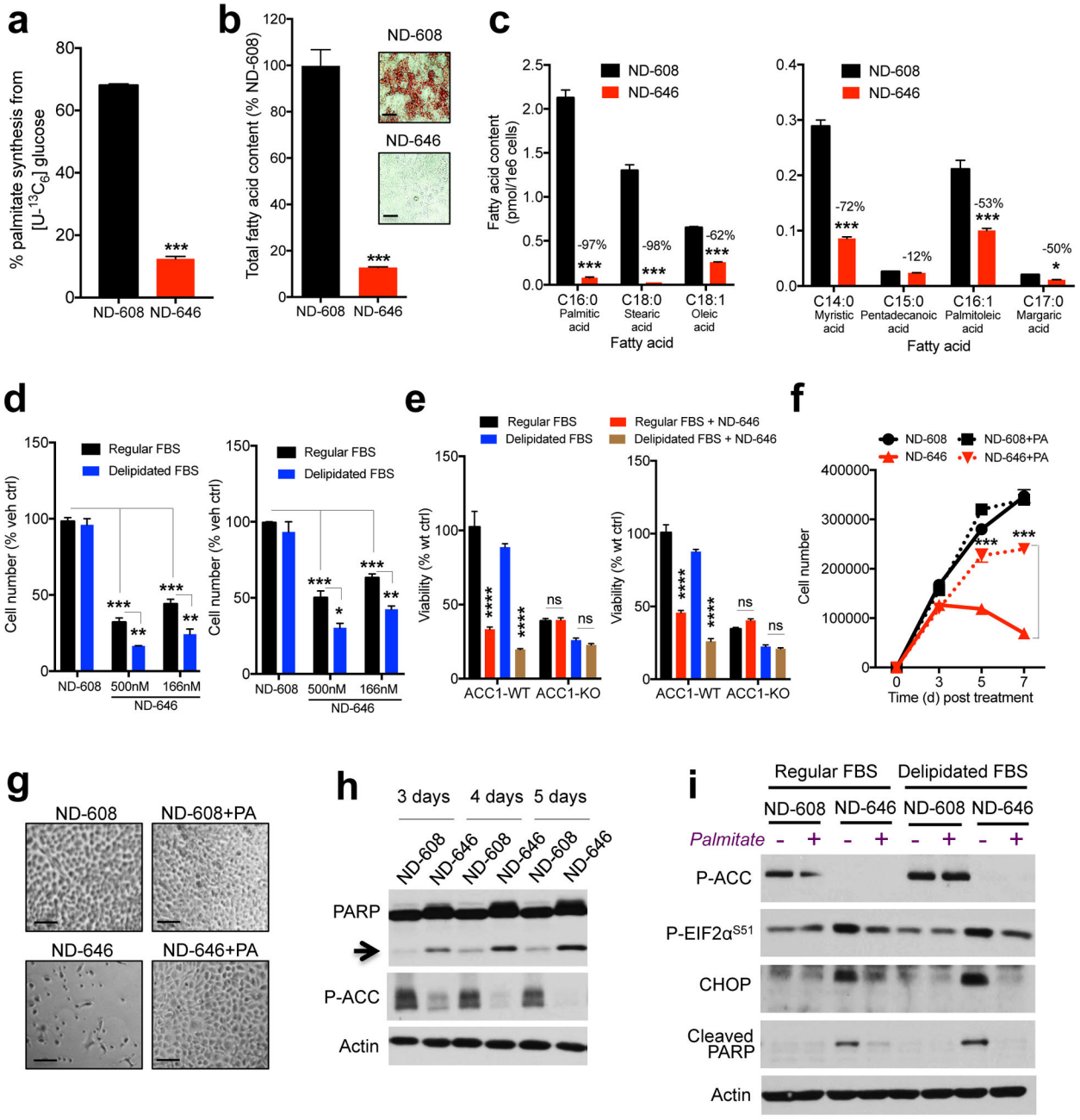

Figure 3. ND-646 inhibits FASyn *in vitro* and induces apoptosis in NSCLC cells

(**a**) Palmitate synthesis in [U-$^{13}C_6$]glucose labeled A549 cells treated with either 500 nM ND-608 or 500 nM ND-646 for 24 hrs.

(**b**) Quantitation of cellular fatty acid content in A549 cells treated with 500 nM ND-608 or 500 nM ND-646 for 72 hrs. Inset images show Oil-Red-O staining of A549 cells. Scale bar = 50 μm

(**c**) Percent reduction of individual fatty acids in A549 cells after 72hrs.

(**d**) Growth of A549 (left) and H460 (right) cells treated with vehicle, 500 nM ND-608 or ND-646 in media containing either regular FBS or delipidated FBS. Cell number shown at day 7-post treatment normalized to percent vehicle.
(**e**) Viability of A549 (left) and H157 (right) WT or *ACC1*-KO clones treated with 500 nM ND-646. Percent viability normalized to WT vehicle.
(**f**) Cellular growth of A549 cells co-treated in delipidated FBS with either 500 nM ND-608 or 500 nM ND-646 and 200 μM palmitate (PA).
(**g**) Images of A549 cells at day 7 post treatment. Scale bar = 50 μm
(**h**) Cleaved PARP expression in A549 cells treated with either 500 nM ND-608 or 500 nM ND-646 in media containing regular FBS at 3, 4 or 5 days post treatment. Arrow denotes molecular weight of cleaved PARP.
(**i**) Palmitate rescue of apoptosis and ER stress in A549 cells co-treated with 200 μM Palmitate and 500 nM ND-608 or 500 nM ND-646 in media containing either regular FBS or delipidated FBS for 5 days..
Technical replicates ranged from three (**a**–**d**) to six (**e**) and are shown from one of at least two separate experiments. All values are expressed as means ± s.e.m. * P<0.05 ** P<0.01 *** P<0.001 **** P<0.001 relative to ND-608 or WT control determined by ANOVA with Tukeys method for multiple comparison (**d**–**f**) or two sided student t test (**a**–**c**).

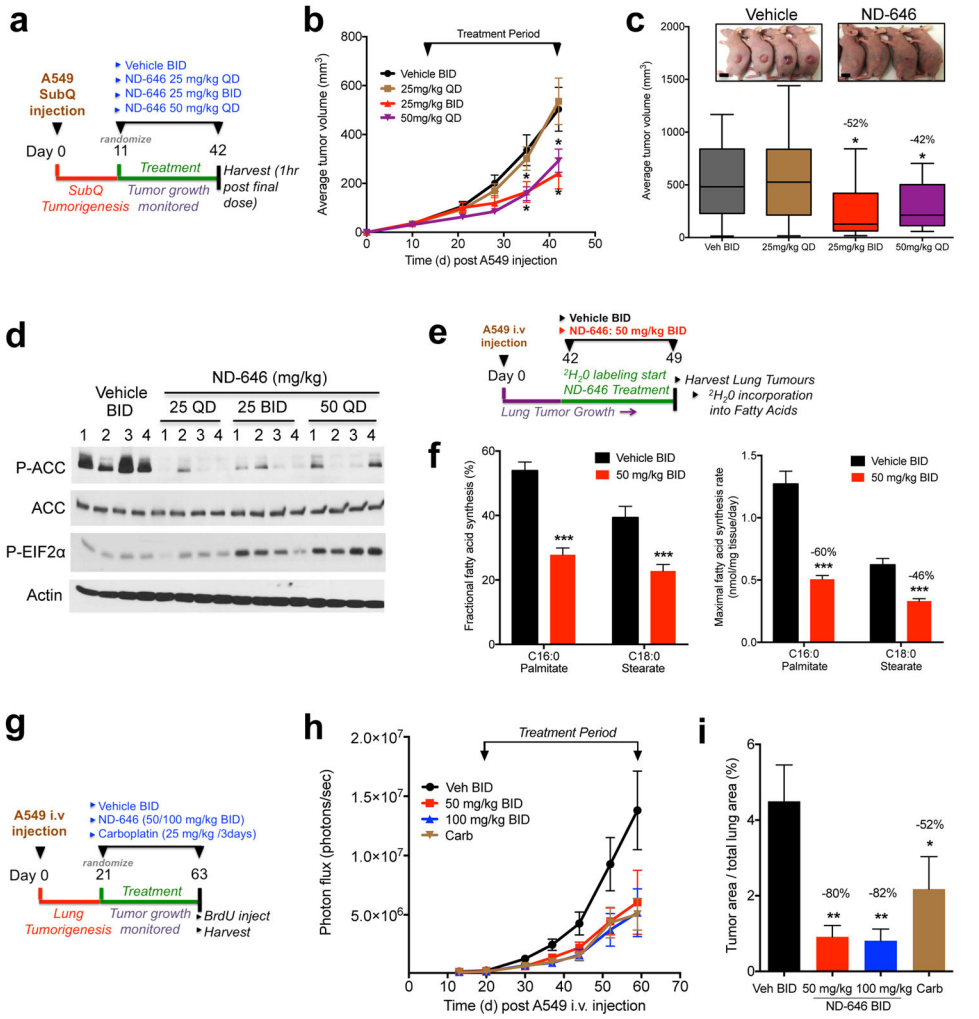

Figure 4. ND-646 inhibits FASyn and tumor growth in NSCLC xenograft models

(**a**) Schematic of ND-646 trial design in A549 subcutaneous tumors

(**b**) Growth of A549 tumors treated with vehicle BID (n=8 mice) or ND-646 at 25 mg/kg QD (n=9 mice), 25 mg/kg BID (n=8 mice) or 50 mg/kg QD (n=10 mice).

(**c**) Box and Whisker plot of tumor volumes at the end of the study (day 42). Inset images are representative from vehicle and ND-646 25mg/kg BID treated mice. Scale bar = 1cm.

(**d**) P-ACC and P-EIF2α^{S51} analysis in A549 tumors. .Numbers represent individual tumors from separate mice.

(**e**) Schematic of $^{2}H_2O$ labeling to measure FASyn in A549 lung tumors (n=4 mice per treatment).

(**f**) Fractional *de novo* palmitate (C16:0) and stearate (C18:0) synthesis (left) and maximal synthesis flux rate (right) is shown in A549 lung tumors (n=12 tumors per treatment)

(**g**) Schematic of ND-646 trial design in A549 xenograft lung tumors.

(**h**) Growth of A549 lung tumors treated with vehicle BID (n=9 mice), ND-646 50 mg/kg BID (n=7 mice), or 100 mg/kg BID (n=9 mice) or Carboplatin (n=9 mice).

(**i**) Quantitation of tumor area as a percentage of total lung area. Average tumor area per treatment is shown.

Numbers in graphs (**c**, **f**, **i**) represent percent decrease compared to vehicle control. All values are expressed as means ± s.e.m. * P<0.05 ** P<0.01 *** P<0.001 relative to vehicle control determined by two sided student t test. Experiments were performed once for each assay.

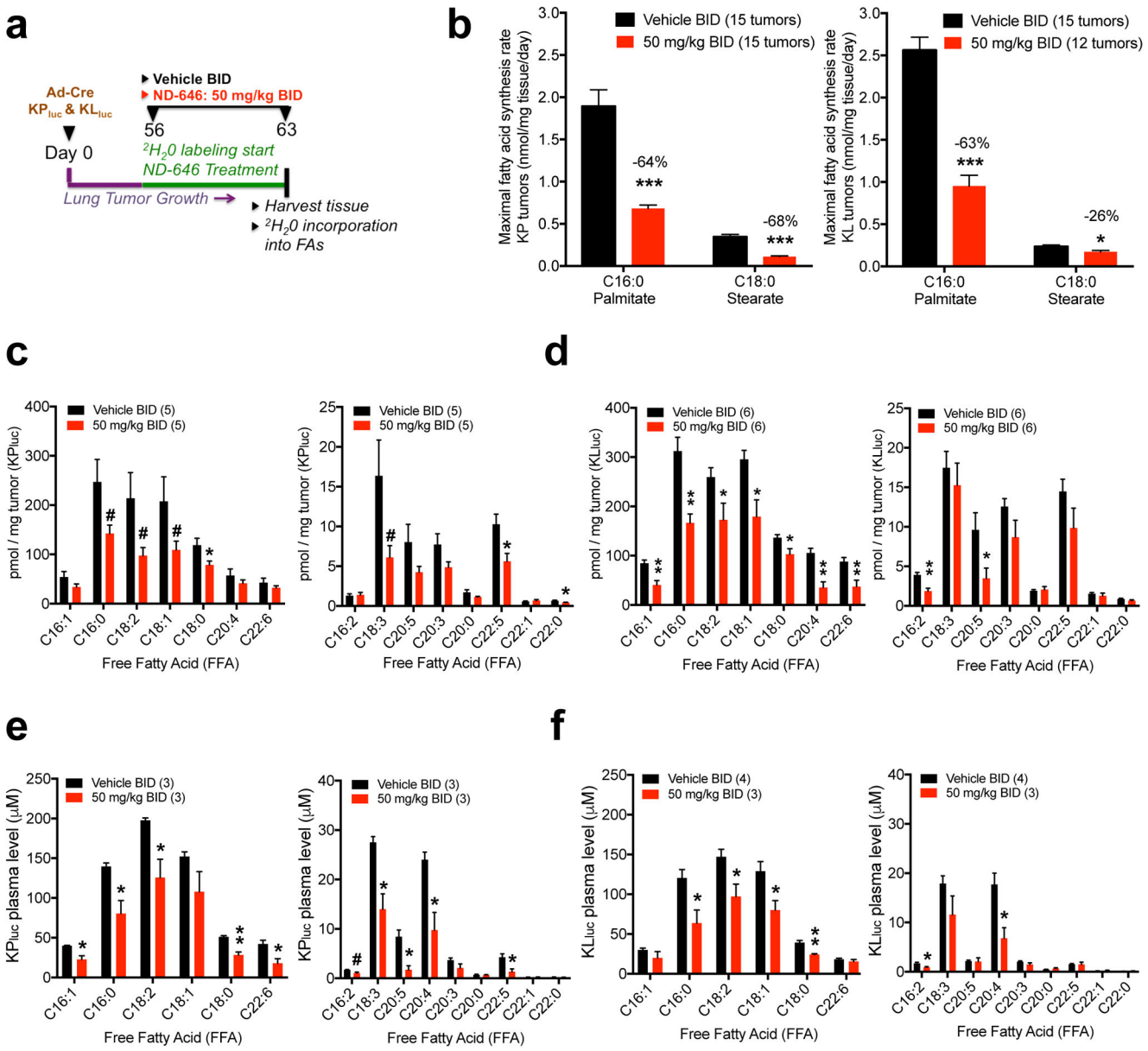

Figure 5. ND-646 inhibits FASyn in lung tumors of Kras^{G12D} p53$^{-/-}$ and Kras^{G12D} Lkb1$^{-/-}$ mouse models of NSCLC and lowers plasma free fatty acids

(**a**) Schematic of $^{2}H_{2}O$ labeling to quantitate FASyn in KP_{luc} and KL_{luc} autochthonous lung tumors (n= 4–5 mice per treatment).

(**b**) Maximal synthesis rate of palmitate (C16:0) and stearate (C18:0) in KP_{luc} lung tumors (left) and KL_{luc} lung tumors (right) after 1 week of ND-646 treatment (PO). 3 tumors per mouse were analyzed. Total number of tumors analyzed is shown in graph. Numbers above bars represent percent decrease compared to vehicle treatment.

(**c**) Quantitation of individual free fatty acids (FFA) in KP_{luc} lung tumors and (**d**) KL_{luc} lung tumors. Left panel shows high abundance FFAs and right panel shows low abundance FFAs.

(**e**) Quantitation of individual free fatty acids (FFA) in plasma from KP_{luc} and (**f**) KL_{luc} mice. Left panel shows high abundance FFAs and right panel shows low abundance FFAs.

Number of tumors and plasma samples analyzed per experiment are shown in graphs. Experiments were performed once for each assay. All values are expressed as means ± s.e.m. * P<0.05 ** P<0.01 *** P<0.001 relative to vehicle treatment determined by two sided student t test. # Represents p values >0.05 p <0.1. Exact p values (**c**–**f**) and % reduction in FFAs are shown in Supplementary Fig. 5e–f.

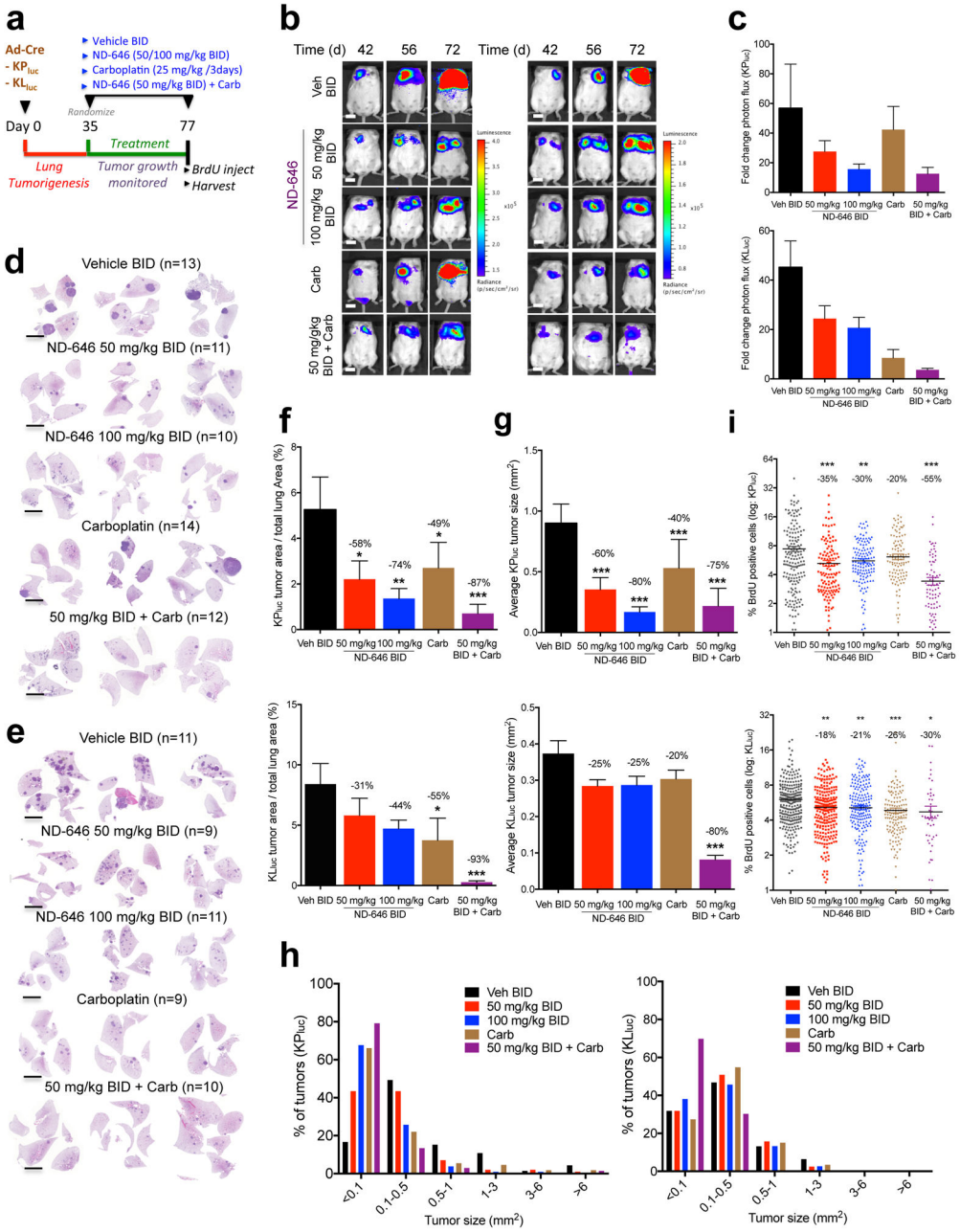

Figure 6. ND-646 suppresses Kras^{G12D} p53$^{-/-}$ and Kras^{G12D} Lkb1$^{-/-}$ autochthonous NSCLC tumor growth

(**a**) Schematic of ND-646 pre-clinical trial design in Kras$^{G12D/+}$ p53$^{fl/fl}$ (KP$_{luc}$) and Kras$^{G12D/+}$ LKB1$^{fl/fl}$ (KL$_{luc}$) genetic NSCLC tumor models

(**b**) Bioluminescence overlay images of ND-646 efficacy in KP$_{luc}$ (left) and KL$_{luc}$ (right) lung tumors. Images are representative for each treatment condition. Scale bar = 1cm.

(**c**) Fold change in photon flux for each group during the treatment period (day 35 to day 77). KP$_{luc}$ (top) and KL$_{luc}$ (bottom).

(**d**) Representative H&E stained sections of KP_{luc} and (**e**) KL_{luc} lung tumors from each treatment group. Number of animals (n) per treatment condition is shown. Scale bar = 5000 μm

(**f**) Tumor burden analysis in KP_{luc} (top) and KL_{luc} (bottom) treated mice. Tumor area was calculated as a percentage of total lung area. Average tumor area per treatment is shown.

(**g**) Average tumor size (mm^2) in KP_{luc} (top) and KL_{luc} (bottom) mice.

(**h**) KP_{luc} (left) and KL_{luc} (right) tumors binned by size (from **g**) and percent of tumors within in each size bin represented per treatment condition.

(**i**) BrdU positivity of KP_{luc} (top) and KL_{luc} (bottom) tumors from each treatment (log2 scale). % BrdU positive cells per tumor was quantified and each dot represents an individual tumor (n=48–262 tumors per treatment).

Number of mice per treatment group shown in (**d**, **e**). For (**g**-**h**) number of tumors analyzed ranged from 46 to 327 based on treatment condition (see source data). All values are expressed as means ± s.e.m. * P<0.05 ** P<0.01 *** P<0.001 relative to vehicle control determined by Mann Whitney test (**f**, **g**) or ANOVA with Tukeys method for multiple comparison (**i**).